Supplementary Information

Fates and spatial variations of accumulation mode particles in a multi-zone indoor environment during the HOMEChem campaign

Erin K. Boedicker[1], Ethan W. Emerson[2], Gavin R. McMeeking[2], Sameer Patel[3], Marina E. Vance[3], Delphine K. Farmer[1*]

[1]Department of Chemistry
Colorado State University
200 W Lake St.
Fort Collins, CO 80523, USA

[2]Handix Scientific LLC
5485 Conestoga Court, Suite 104B
Boulder, CO 80301, USA

[3]Department of Mechanical Engineering
University of Colorado Boulder
111 Engineering Drive, 427 UCB
Boulder, CO 80309, USA

Number of pages: 27

Number of figures: 19

Number of tables: 13

CONTENTS

Section S1: Instrument diagnostics and data treatment

S1.1: Instrument background intercomparisons

We conducted intercomparisons over four days of the HOMEChem campaign, at the beginning from 1 June to 3 June and then in the middle of the campaign on 23 June, during which the four POPS were co-located with each other and the UHSAS. Both of these periods correspond to background when no activities were going on in the house. The POPS were stacked together with approximately 10 to 24 cm between inlets and were placed on a counter space <1m from the UHSAS inlet. No corrections were done in response to these intercomparisons.

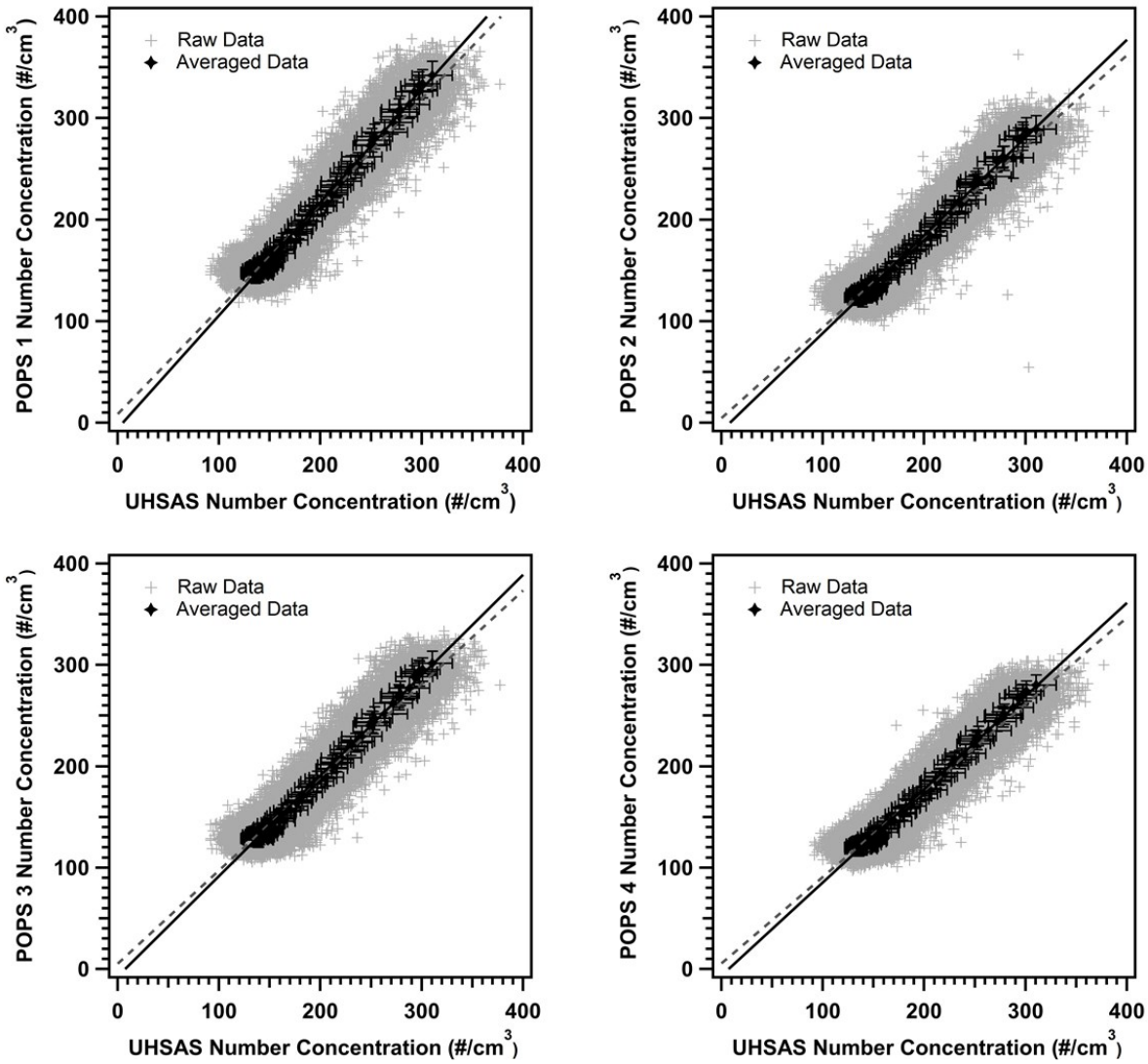

Figure S1: Comparison of number concentration sub-range between the overlapping size regions of the four POPS and the UHSAS showing good correlations between the instruments. The 1-second data is in grey and the 5-minute average of the data is in black in all the plots.

Table S1: Fit equations and R^2/ X^2 values for the POPS to UHSAS intercomparisons. In the table, the fit to the 1-second data is listed first and the fit to the 5-minute average is listed second in bold with a X^2 instead of an R^2 because of the presence of x and y error from the averaging.

Instruments	Slope	Int.	R^2 / $\mathbf{X^2}$
POPS 1 vs UHSAS	1.035 ± 0.002	8.7 ± 0.4	0.901
	1.11 ± 0.04	**-6 ± 8**	**1.54**
POPS 2 vs UHSAS	0.893 ± 0.002	4.5 ± 0.4	0.898
	0.96 ± 0.04	**-8 ± 7**	**1.97**
POPS 3 vs UHSAS	0.920 ± 0.002	5.4 ± 0.4	0.898
	0.99 ± 0.04	**-7 ± 7**	**1.70**
POPS 4 vs UHSAS	0.853 ± 0.002	5.5 ± 0.3	0.902
	0.92 ± 0.04	**-6 ± 6**	**1.72**

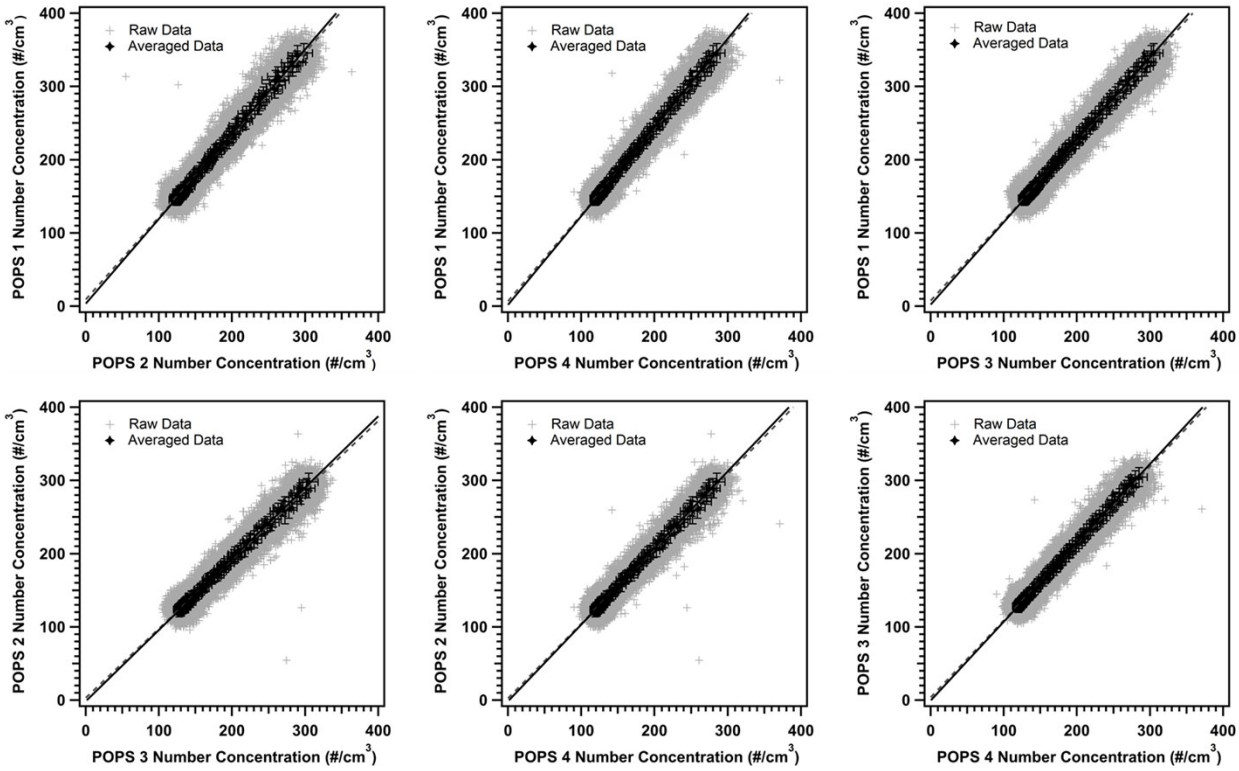

Figure S2: Comparison of number concentration between the four POPS showing good correlations between the instruments during background periods (average comparison slope of 1.0694 ±0.0006).

Table S2: Fit equations and R^2/ X^2 values for the POPS vs POPS intercomparisons. In the table, the fit to the 1-second data is listed first and the fit to the 5-minute average is listed second in bold with a X^2 instead of an R^2 because of the presence of x and y error from the averaging.

Instruments	Slope	Int.	R^2 / X^2
POPS 1 vs POPS 2	1.124 ± 0.001	9.3 ± 0.3	0.947
	1.16 ± 0.03	**4 ± 5**	**2.30**
POPS 1 vs POPS 3	1.095 ± 0.001	7.6 ± 0.3	0.950
	1.13 ± 0.03	**2 ± 5**	**0.568**
POPS 1 vs POPS 4	1.181 ± 0.001	6.9 ± 0.2	0.951
	1.21 ± 0.03	**2 ± 5**	**0.662**
POPS 2 vs POPS 3	0.945 ± 0.001	3.4 ± 0.2	0.945
	0.97 ± 0.03	**-1 ± 4**	**1.65**
POPS 2 vs POPS 4	1.021 ± 0.001	2.7 ± 0.2	0.948
	1.05 ± 0.03	**-1 ± 4**	**1.82**
POPS 3 vs POPS 4	1.051 ± 0.001	3.9 ± 0.2	0.950
	1.08 ± 0.03	**-1 ± 4**	**0.432**

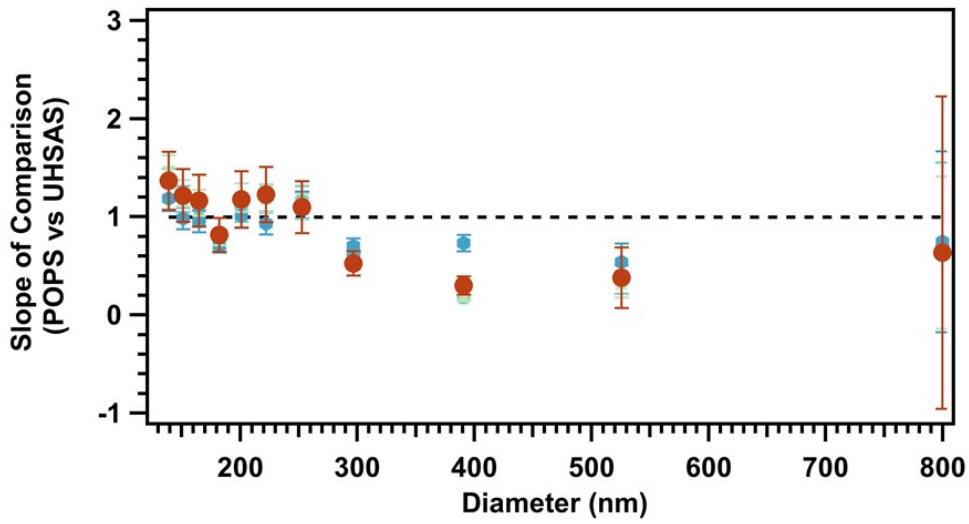

Figure S3: Size-dependent comparison of number concentration between re-binned UHSAS and POPS data which shows that there is an inherent offset between the size ranges on the two instruments. The POPS slightly overestimate particles in their lower range and underestimate particles at the upper end of their range when compared to the UHSAS. Comparisons between each POPS and the UHSAS are represented by the blue points; the orange points are the average slope values from all four POPS.

S1.2: Instrument intercomparisons during cooking

On 23 June, after the second round of background intercomparisons, the fourth POPS was placed bellow the UHSAS inlet in the kitchen and left there for the remainder of the campaign. Data collected from a breakfast, stir-fry, and chili cooking on 25 June was compared for the overlapping size range (0.13 – 1 μm) of the two instruments (**Table S6**, **Figure S7**). The

POPS was shown to be responsive to the sharp changes in aerosol concentration, given that there was no delay time between the UHSAS and POPS response to cooking. Although the maximum concentration listed by the manufacturer for the POPS is 1,250 # cm^{-3} the POPS used in the comparison showed good agreement with the UHSAS at higher concentrations. While noise in the POPS measurement increased at these elevated concentrations, averaging the data (1-minute averages in the comparisons) resolved this and resulted in similar results as those obtained from the background intercomparisons.

The two optical instruments were also compared against an SMPS present during the campaign. Using the same data from 23 June data from each cooking type was compared from the overlapping size ranges (0.06 – 0.535 µm for the UHSAS and 0.134 – 0.455 for the µm POPS) (**Table S3**, **Figure S4**). The comparisons indicate that average number distributions measured by the instruments are comparable, which validates the use of these optical instruments for the size dependent analysis presented. There was disagreement in the smallest sizes of the UHSAS distribution, however, this data was not used in the spatial analysis presented. Additionally, deposition of particles < 100 nm is not presented because of saturation (discussed in the next section) therefore excluding the size region that had the largest difference from the SMPS's number distribution. The comparisons do indicate that the optical instruments underestimate total particle number concentrations during the cooking events. Underestimation is likely a result of differences in the composition and therefore refractive index of cooking particles and the PSL's used to calibrate the instruments as well as saturation effects during cooking. This does not impact this work because the focus here is not on characterizing the total cooking emissions.

Table S3: Fit equations and R^2/ X^2 values for the POPS vs UHSAS vs SMPS intercomparisons during cooking. In the table, the fit to the 1-second data is listed first and the fit to the 1-minute average is listed second in bold with a X^2 instead of an R^2 because of the presence of x and y error from the averaging. Background comparison from POPS 4 vs UHSAS is included in the first column for context.

Instruments		Background	Breakfast	Stir-Fry	Chili
POPS vs UHSAS	*Slope*	0.853 ± 0.002	0.766 ± 0.007	0.803 ± 0.009	0.573 ± 0.006
		0.92 ± 0.04	**0.92 ± 0.04**	**0.87 ± 0.02**	**0.83 ± 0.08**
	Int.	5.5 ± 0.3	29 ± 2	-10 ± 20	132 ± 3
		-6 ± 6	**-10 ± 10**	**-2 ± 8**	**20 ± 30**
	R^2 / $\mathbf{X^2}$	0.902	0.928	0.854	0.740
		1.72	**2.65**	**83.8**	**9.58**
POPS vs SMPS	*Slope*		0.55 ± 0.08	0.62 ± 0.01	0.5 ± 0.1
	Int		-140 ± 50	-22 ± 9	20 ± 60
	X^2		**10.9**	**2.07**	**5.23**
UHSAS vs SMPS	*Slope*		0.43 ± 0.04	0.427 ± 0.005	0.51 ± 0.06
	Int.		-10 ± 50	260 ± 40	100 ± 200
	X^2		**1.49**	**34.8**	**22.3**

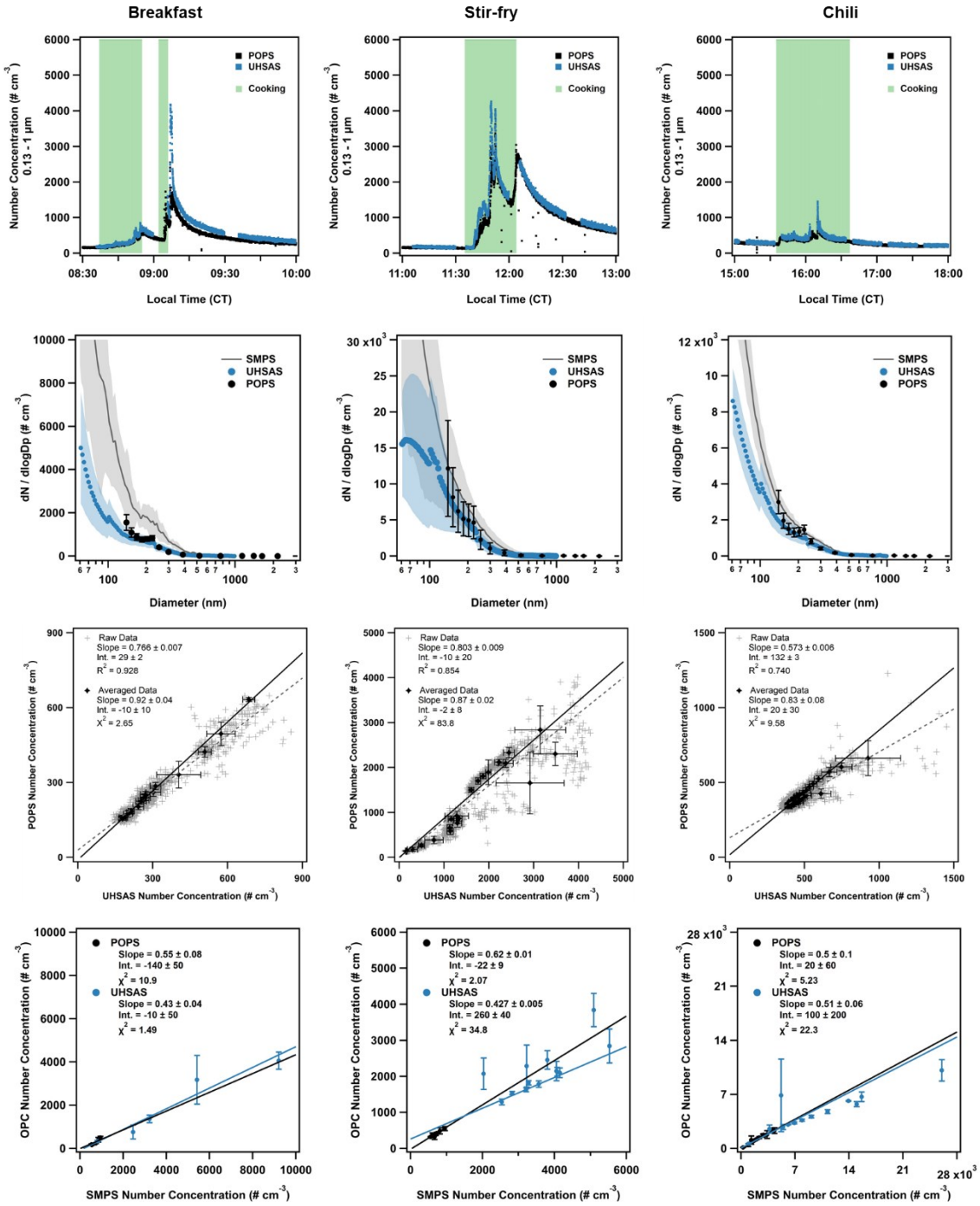

Figure S4: A sub-plot of each cooking event that had enough data to be used for intercomparisons (breakfast, stir-fry, and chili) are presented on the **top row** followed by distribution comparisons in the **second row,** intercomparison plots between the POPS and UHSAS data in the **third row**, and intercomparison plots between the optical particle counters (OPC) and the SMPS in the **fourth row**. The events are in order of the time they were done during the experiment day from left to right in the plots. In the POPS vs UHSAS intercomparison plots raw 1-second data is presented as grey, with the dashed line being the raw

intercomparison line, and 1-minute averaged data is presented in black, with the solid line being the intercomparison line. In the OPC vs SMPS the black traces are for the POPS and the blue traces are for the UHSAS.

S1.3: Saturation of optical instruments at high concentrations

At high aerosol concentrations, optical instruments will saturate causing the instruments to undercount particles. We present a brief analysis of those saturation levels through comparison of the aerosol number concentration of the two instruments to the SMPS that was present during the HOMEChem study. The analysis uses the end of the day decay period from the two Thanksgiving experiments conducted during the campaign (2018/06/18 and 2018/06/27) because it was a period during which the aerosol concentration decayed naturally (no intentional venting) from an extremely elevated level back to background while the house was unoccupied. For the POPS analysis, data from POPS 1 in the kitchen were used. The comparison shows that the POPS consistently overestimates compared to the SMPS and a saturation level for the instrument cannot be identified. The UHSAS agrees well with the SMPS for concentrations below ~3000 particles cm^{-3} and saturation is a significant problem at concentrations above ~10,000 particles cm^{-3}. This saturation is only affecting the second detector of the USHAS, which measures particles < 240 nm in diameter. For this analysis saturation could lead to slight suppression in the number size distribution below 240 nm, however, saturation does not affect the volume estimations since particles from the first detector (> 240 nm) are what dominate this measurement. Additionally, since saturation leads to underestimation of concentration for particles < 240 nm the measured loss rate of these aerosols is also suppressed. Periods where saturation was affecting the data are identified accordingly in this analysis.

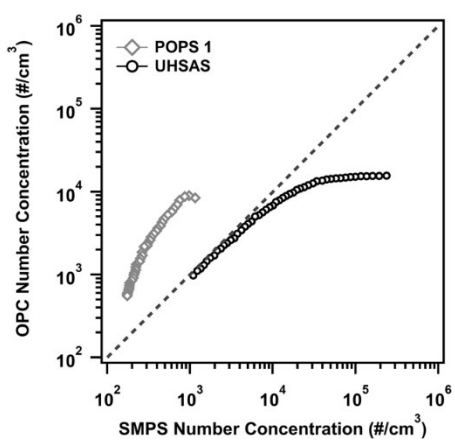

Figure S5: Total concentration from both optical particle counters (OPC) – the UHSAS and POPS – plotted against the total concentration of the SMPS for the size regions that overlapped between the instruments (60 – 530 nm for the UHSAS and SMPS, and 130 – 530 nm for the POPS and SMPS).

S1.4: Data treatment and density assumption

Both instruments assume spherical particles in all number to area, volume, and mass conversions. All the mass measurements reported in the supplementary text used an assumed density of 1.2 g cm^{-3}, which was selected because of the high organic content of the observed cooking-derived particles.[1] Total mass is not the focus of this work and mass measurement approximations are reported only to provide context. We recognize that for cooking aerosols this density is likely an overestimation and for background periods this density is a slight underestimation. Patel et al. (2020) provides a detailed description of aerosol density during the HOMEChem campaign using Aerosol Mass Spectrometer (AMS) data that was available. Patel et al. (2020) report that aerosol density fluctuated between ~1.0 g cm^{-3} during cooking and ~1.5 g cm^{-3} during non-cooking periods. Given this range, we take 1.2 g cm^{-3} as a density for all the data to provide mass estimations of measured aerosols, unless otherwise stated. Unit density (1.0 g cm^{-3}) is used in the model simulations since it involved only cooking aerosol.

Section S2: Summary of the Lai and Nazaroff (2000) Indoor Deposition Model

Tables S3 – S5 summarize the variables and equations used by the Lai and Nazaroff (2000) to calculate deposition velocity and loss rate of indoor aerosols. The information presented is a recreation of the equation summary tables presented in the original paper.

Table S4: Variables used in the Lai and Nazaroff (2000) model.

Variable	Definition	Set Value
d_p	Particle diameter	
$\boldsymbol{u}$	Friction velocity	1 m/s
$\boldsymbol{\rho_p}$	Particle density	1000 kg m^{-3}
v_s	Gravitational settling velocity	
v	Kinematic viscosity of air	
D	Brownian diffusivity of the particle	
$\mathbf{A_v}$ †	Area of vertical surfaces	250 m^2
$\mathbf{A_u}$ †	Area of upward-facing surfaces	111 m^2
$\mathbf{A_d}$ †	Area of downward-facing surfaces	111 m^2
V †	Volume of the room	250 m^3

† These values are from the house measurements listed in the HOMEChem overview paper [4].

Table S5: Equations used in the Lai and Nazaroff (2000) model.

Parameters	Equation
Integral †	$I = \left[3.64\, Sc^{2/3}\,(a - b) + 39\right]$ $a = \frac{1}{2}\ln\left[\frac{\left(10.92\, Sc^{-1/3} + 4.3\right)^3}{Sc^{-1} + 0.0609}\right] + \sqrt{3}\tan^{-1}\left[\frac{8.6 - 10.92\, Sc^{-1/3}}{\sqrt{3}\, 10.92\, Sc^{-1/3}}\right]$ $b = \frac{1}{2}\ln\left[\frac{\left(10.92\, Sc^{-1/3} + r^{+}\right)^3}{Sc^{-1} + 7.669 \times 10^{-4}\left(r^{+}\right)^3}\right] + \sqrt{3}\tan^{-1}\left[\frac{2\, r^{+} - 10.92\, Sc^{-1/3}}{\sqrt{3}\, 10.92\, Sc^{-1/3}}\right]$
Schmidt number (*Sc*)	$Sc = v\, D^{-1}$
r^{+}	$r^{+} = d_p\, u^{*}\,(2v)^{-1}$
Deposition velocity, vertical surface	$v_{dv} = \frac{u^{*}}{I}$
Deposition velocity, upward horizontal surface	$v_{du} = \frac{v_s}{1 - exp\left(-\frac{u_s I}{u^{*}}\right)}$
Deposition velocity, downward horizontal surface	$v_{dd} = \frac{v_s}{exp\left(\frac{u_s I}{u^{*}}\right) - 1}$
First-order loss coefficient for deposition, rectangular cavity	$\beta = \frac{v_{dv}A_v + v_{du}A_u + v_{dd}A_d}{V}$

† Evaluated using the approximation that Brownian diffusivity is negligible compared to the eddy diffusivity. This approximation is valid for diameters larger than 0.01 μm. For smaller particles, a numeric integration is required (see Table S9).

Table S6: Numeric integration of the integral (*I*), done by Lai and Nazaroff (2000).

Particle Diameter, d_p (μm)	Integral, I (–)
0.001	29.1
0.0015	49.1
0.002	71.0
0.003	120.3
0.004	174.9
0.005	234.2
0.006	297.4
0.007	364.0
0.008	432.7
0.009	504.5
0.01	579.3

Section S3: Summary of the Emerson Outdoor Deposition Model

Tables S6 and S7 summarize the variables and equations used by Emerson et al. (2020) to calculate deposition velocity and loss rate of aerosols, as well as the variables we selected to represent the indoor environment. These calculations are a modification of the Zhang et al. (2001) model.

Table S7: Variables used by Emerson et al. (2020). The constants in this table are bolded and the value they were set to for the indoor environment are in the last column of the table.

Variable	Definition	Set Value
d_p	Particle diameter	
$\boldsymbol{u}^{\square}$	Friction velocity	0.02 m s^{-1}
v	Kinematic viscosity of air	
D	Brownian diffusivity of the particle	
C	Cunningham slip correction factor	
$\boldsymbol{u_H}$	Windspeed	0.1 m s^{-1}
$\boldsymbol{\rho_p}$	Particle density	1000 kg m^{-3}
$\boldsymbol{z_r}$	Hight of deposition measurement	2 m
LUC**	Land use category	1
SSC**	Seasonal select category	1
z_0 †	Roughness length	0.8 m
A †	Characteristic radius of collectors	2.0 mm
$\boldsymbol{\varepsilon_0}$	Empirical constant for surface resistance	3
γ †, ‡	Brownian constant	0.56
$\boldsymbol{C_B}$ ‡	Empirical constant for Brownian	0.3

α †	Impaction constant	1.0
β ‡	Empirical constant for impaction	0.6
$\mathbf{C_{Im}}$ ‡	Empirical constant for impaction	0.1
υ ‡	Empirical constant for interception	1
$\mathbf{C_{In}}$	Empirical constant for interception	2.5

**The LUC and SSC follow the numbering system used in Zhang et al. (2001), which parameterized 15 land use categories and 5 seasonal categories.

†These parameters are dependent on the LUC and the SSC. The value tables for these parameters are listed in Zhang et al. (2001), the values listed here are the ones associated with the LUC and SSC that were used in this analysis.

‡ These parameters were altered from the Emerson et al. (2020) model to better represent the indoor data.

Table S8: Summary of main equations used in the Emerson et al. (2020) model.

Parameters	Equation
Deposition velocity (V_d)	$V_d = V_g + \frac{1}{(R_a + R_s)}$
Gravitational settling velocity (V_g)	$V_g = \frac{\rho_p \, d_p^{\,2} \, g \, C}{18 \, \eta}$
Aerodynamic resistance above the canopy (R_a)**	$R_a = \frac{\ln\left(\frac{z_r}{z_0}\right) - \psi_H}{\kappa \, u^*}$
Surface resistance (R_S)	$R_s = \frac{1}{\varepsilon_0 \, u^* \, (E_b + E_{im} + E_{in}) R_1}$
Collection efficiency from Brownian diffusion (E_b)	$E_b = C_B Sc^{-\gamma}$
Collection efficiency from impaction (E_{im})	$E_{im} = C_{Im}\left(\frac{St}{\alpha + St}\right)^{\beta}$
Collection efficiency	

from interception (E_{in})	$E_{in} = C_{In}\left(\frac{d_p}{A}\right)^{v}$
Bounce correction factor	$R_1 = exp(-St^{0.5})$
Schmidt number (Sc)	$Sc = v\,D^{-1}$
Stokes number (St)	$St = \frac{V_g\,u^*}{g\,A}$

**For the indoor environment this term is used to represent the conditions of the air above the sample inlet. The stability function (ψ) was set to zero for the indoor environment.

Section S4: Experimental days and background conditions during HOMEChem

When no activities are performed indoors and all external doors and windows are closed, penetration of outdoor particles into the building is the most significant source of indoor particles. Out of the three main indoor events simulated during the HOMEChem campaign (i.e. cooking, cleaning, and human occupancy), cooking produced the largest concentration of submicron particles (**Figure S14**).

During background periods, the UHSAS (60 – 1000 nm) measured an indoor concentration of 175.2 ± 0.5 particles cm^{-3} (~1.4 ± 0.3 μg m^{-3}) during the day and 100.2 ± 0.4 particles cm^{-3} (~ 0.8 ± 0.2 μg m^{-3}) at night. Particle concentrations and size distributions were homogeneous (concentration within 18%) throughout the house, and no inherent gradient was observed between rooms (**Figure S15**). Trends in indoor particle concentration mirrored those observed outdoors (**Figure S15**). Both the indoor and outdoor size distributions were bimodal with similar modes but differences in overall magnitude (**Figure S15**). This similarly indicates that the indoor particle concentrations during background periods are dominated by infiltration of outdoor particles, consistent with previous findings.[7–12]

Particle infiltration can be characterized by the ratio between indoor and outdoor (I/O ratio) particle concentrations when the house is closed. This I/O ratio is 0.5 ± 0.1 for number concentration (0.6 ± 0.9 for mass concentration) of submicron particles (**Figure S15**). The I/O ratio varies according to particle size, with ultrafine (< 100 nm) and coarse (> 1 μm) mode particles penetrating least effectively and accumulation mode particles (100 nm – 1 μm) entering most freely with the peak in I/O around 150 nm (**Figure S15**). This trend is the result of diffusion losses due to Brownian motion dominating small particles and gravitational settling forces, impaction, and interception dominating larger particles, causing both modes to deposit in the ventilation system and be removed when moving through the building envelope. For submicron particles, the average I/O ratio is 0.74 ± 0.02. Size-dependent I/O ratios published by

Zhao et al. (2019) and Hussein et al. (2005) both showed the same trend with peaks in I/O at 100 – 200 nm. In the context of this work, the I/O ratio represents a general relationship that can be used to investigate the dominating sources of particles indoors.

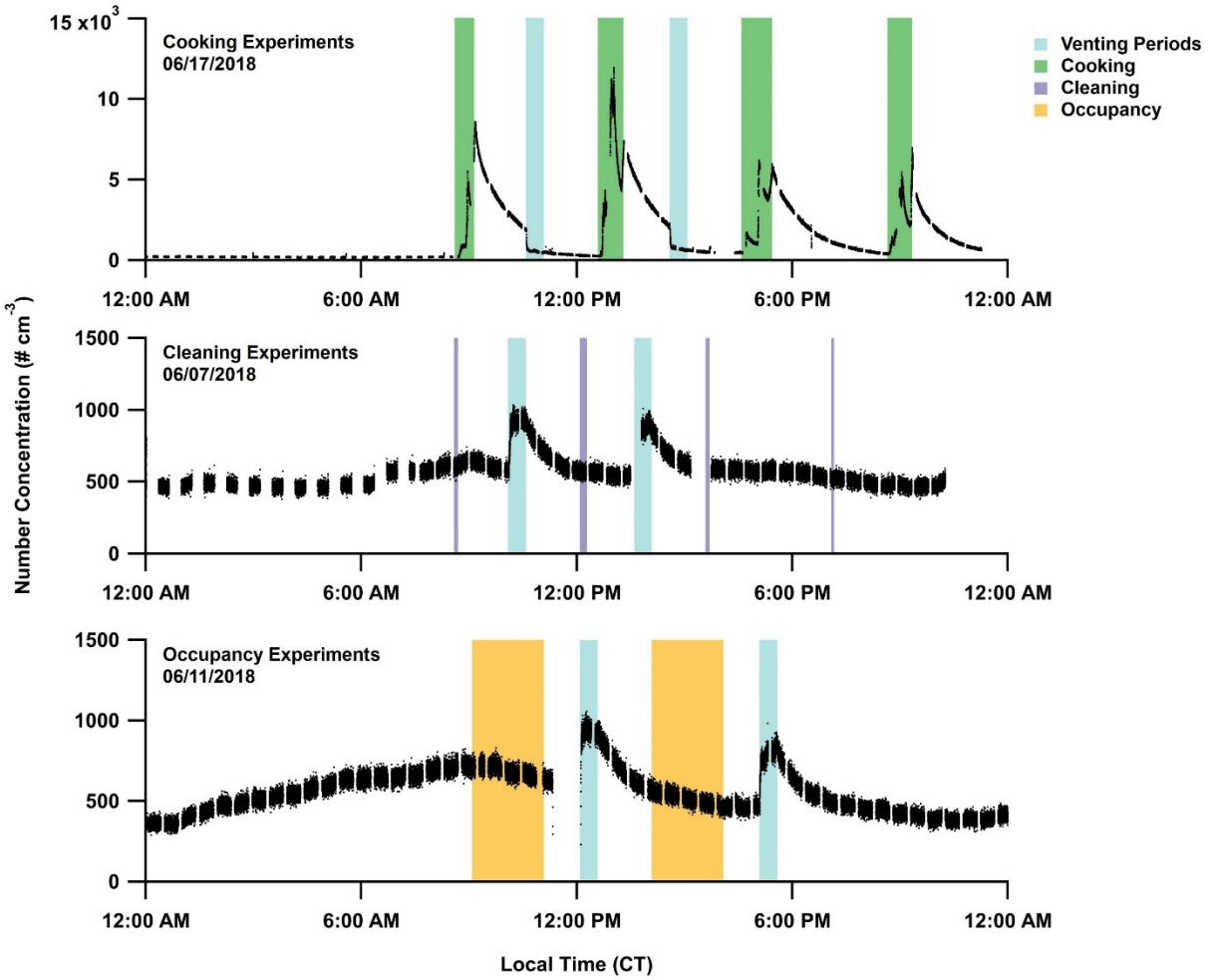

Figure S6: Time-series of three full sequential days when cooking (top), cleaning (middle), and human occupancy (bottom) experiments were done in the house. Cooking had the largest number of particles reported, while cleaning and human occupancy did not show a substantial increase above the background concentration for the particle range sampled (60 – 1000 nm).

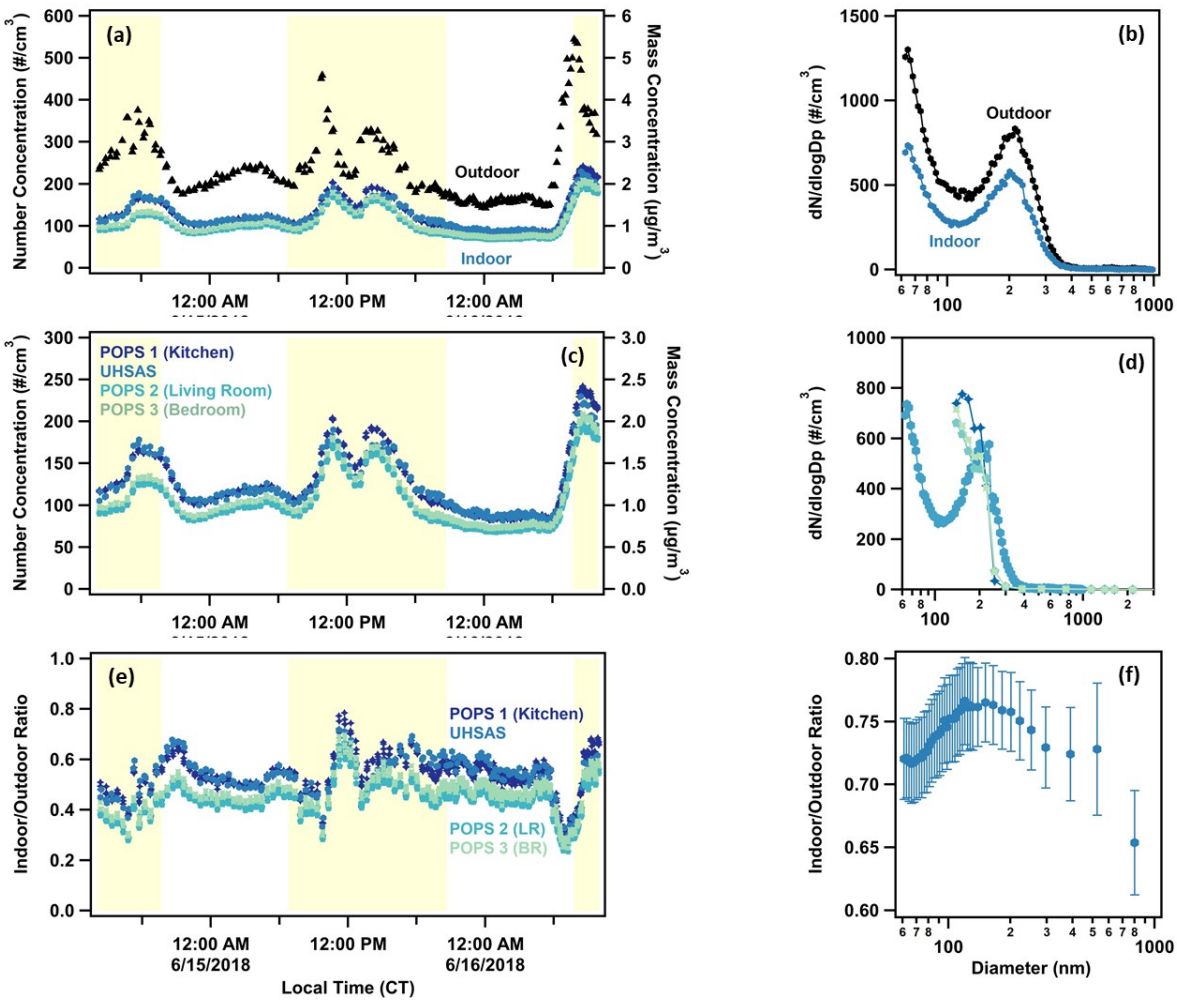

Figure S7: (a) Indoor and outdoor aerosol concentrations during a background period. (b) Size distribution of aerosols indoors and outdoors during background. (c) During background periods there were no significant gradients present throughout the house, even during the daytime periods (highlighted regions) when aerosol concentration spiked. (d) The distribution was also consistent across the house during these periods. (e) Ratio of indoor to outdoor aerosol concentration at all four sampling points. (f) Size-dependent indoor to outdoor aerosol concentration ratio.

Section S5: Aerosol concentrations and distributions during cooking

During all cooking events, particle number concentration indoors increased to at least ten times the indoor background concentration, and at least six times higher than the measured outdoor concentration. Stir-fry events resulted in peak number concentrations, measured by the UHSAS, of approximately 5200 ± 300 particles cm^{-3} (25 ± 2 μg m^{-3}), breakfast events had concentrations of 10800 ± 600 particles cm^{-3} (19.9 ± 0.9 μg m^{-3}), and chili cooking events had an average peak concentration of 5000 ± 300 particles cm^{-3} (14.4 ± 0.6 μg m^{-3}). Toasting bread produced the largest peak number concentration of particles at 12400 ± 500 particles cm^{-3} (16.8 ± 0.8 μg m^{-3}). All the cooking events produced high concentrations of fine and ultra-fine particles, with an average count median diameter of 110 ± 10 nm for all cooking. Median diameters were relatively consistent through emission periods except for some stir-fry events, which exhibited a change in their distribution during emission periods (**Table S9, Figure S9**).

S5.1: Distribution characteristics for the different cooking events

Table S9: Median diameters of aerosol distributions observed by the UHSAS during HOMEChem cooking events

Cooking Event	CMD (nm)	SMD (nm)	VMD (nm)
Breakfast	98 ± 7	126 ± 9	140 ± 10
Toast	99 ± 6	123 ± 8	136 ± 7
Stir-fry**	110 ± 10	180 ± 20	230 ± 20
Chili	101 ± 9	140 ± 10	170 ± 20
Total Cooking	110 ± 10	150 ± 20	180 ± 20

**This represents an overall average distribution during the stir-fry cooking events, however, some of the stir-fry events had a shift in the distribution during the event that resulted in different CMD values (see section S – 3.2).

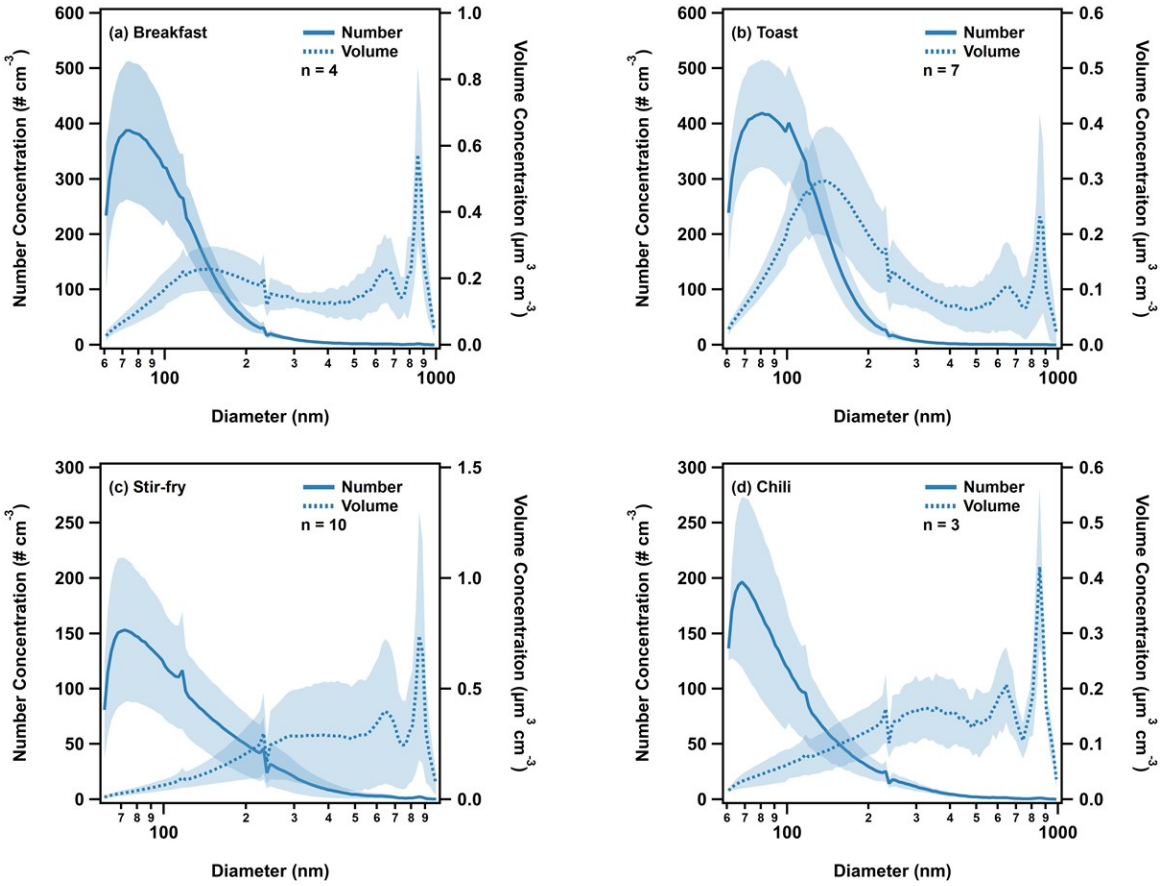

Figure S8: Average distributions for the different cooking events: (a) breakfast, (b) toast, (c) stir-fry, and (d) chili. Each plot has number distribution (dN) on the left, represented by the solid trace, and volume distribution (dV) on the right, represented by the dashed trace. The shaded region on the plots represents the standard deviation of the distributions. The seam at 240 nm is an artifact of the two-detector system on the UHSAS, and this point represents the switching point between the two instruments. In these distributions, both the breakfast and the toast sub 240 nm number concentrations are likely underestimated as a result of saturation.

S5.2: Distribution shifts during select stir-fry events For all the stir-fry experiments, two main peaks in concentration were observed (**Figure S9**). Out of the stir-fry experiments done, six of the events showed a shift in the distribution during the second peak in concentration. This is likely due to a change in the emission during these events.

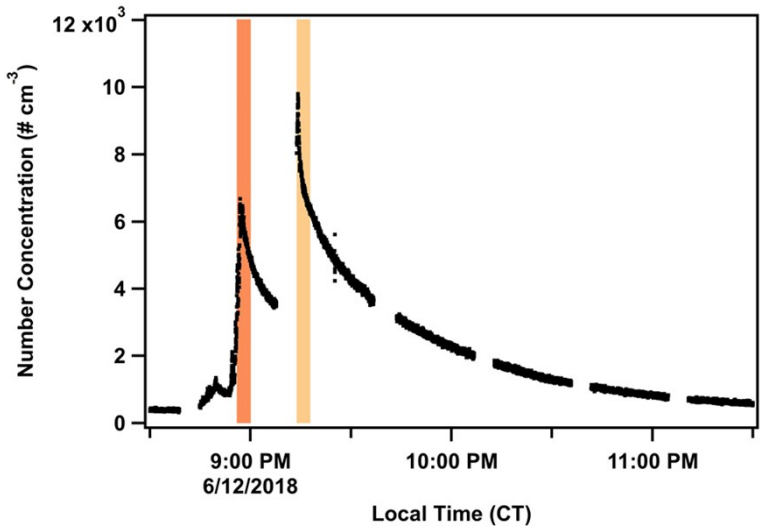

Figure S9: Time series of total number concentration (dN) from the UHSAS showing the typical trend observed during stir-fry events. In six of the observed stir-fry experiments, the aerosol size distributions between these two peaks changed substantially. This stir-fry event from 12th June was one of the stir-fry experiments that exhibited this change in emission.

Table S10: Median diameters of aerosol distributions observed for the different periods during a stir-fry event and the overall median diameter of the event

Stir-fry Period	CMD (nm)	SMD (nm)	VMD (nm)
First Peak	110 ± 10	160 ± 20	200 ± 20
Second Peak	134 ± 6	222 ± 9	290 ± 10
Total Stir-Fry	110 ± 10	180 ± 20	230 ± 20

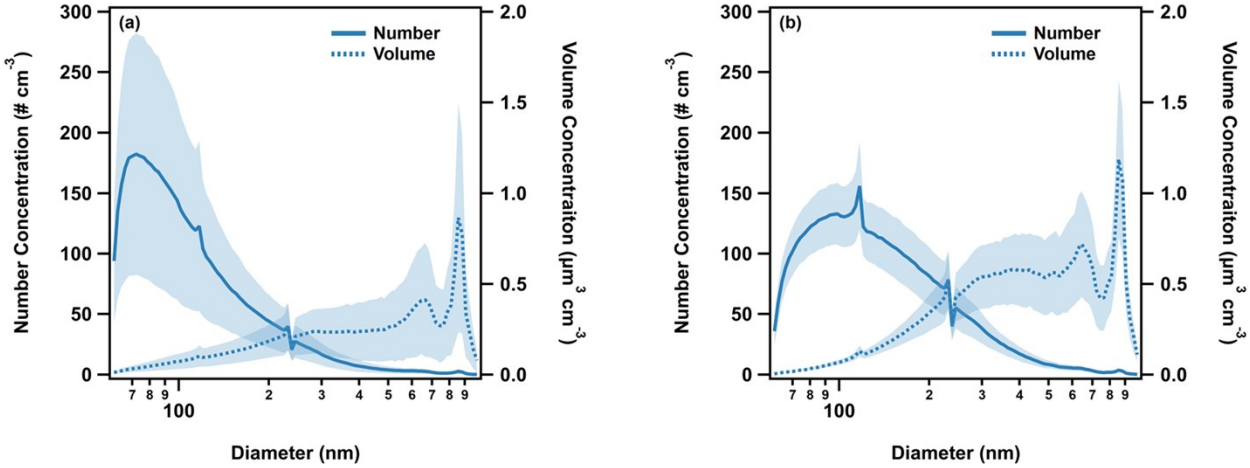

Figure S10: Average distributions for the two peaks during a stir-fry event: (a) first peak and (b) second peak. Both plots have number distribution on the left, the solid trace, and volume distribution on the right, the dashed trace. The shaded region on the plots represents the standard

deviation of the distributions. The seam at 240 nm is an artifact of the two-detector system on the UHSAS, and this point represents the switching point between the two instruments.

Section S6: Loss of cooking aerosol

S7.1: Measured loss rate for cooking aerosols

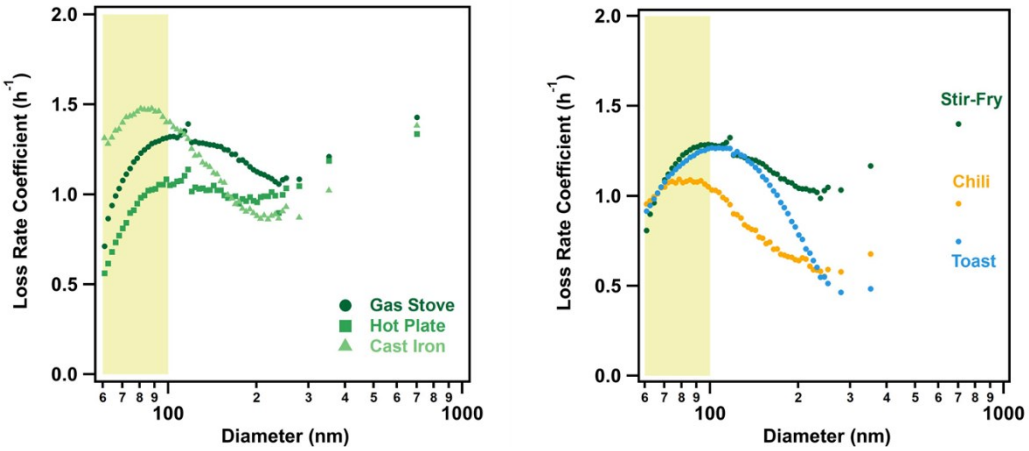

Figure S11: Measured loss rates for the different stir-fry types (left) and the different types of cooking events (right). The size-dependent loss rates for the three types of stir-fries and the different cooking events were not substantially different from each other. The highlighted region of both plots represents the data below 100 nm that was heavily affected by saturation of one of the UHSAS detectors, leading to suppressed concentration peaks and loss rates.

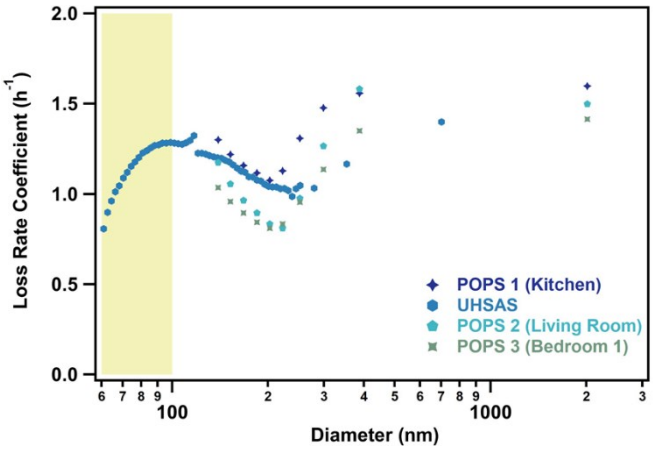

Figure S12: Measured loss rates at the four measurement points throughout the house. The highlighted region in the figure represents data that was heavily affected by UHSAS saturation, leading to suppressed concentration peaks and loss rates. No significant variation was observed between rooms for the aerosol loss rate.

S7.2: Deposition velocity and rate

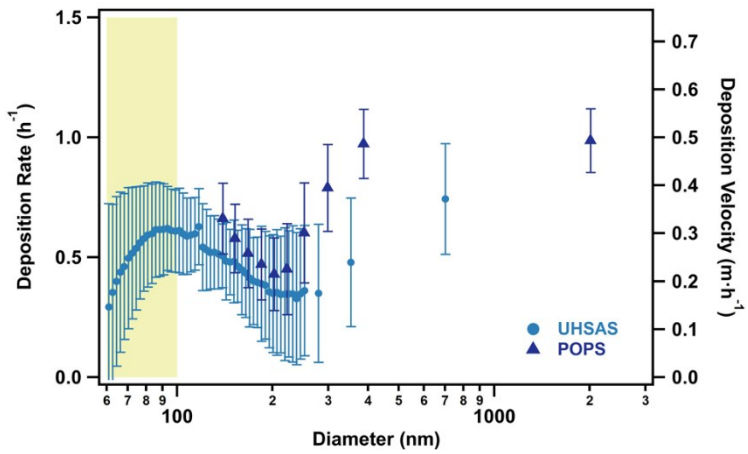

Figure S13: Total average deposition rate and deposition velocity for all HOMEChem cooking events from the UHSAS and the POPS. Error bars represent the standard deviation of the measured deposition across the different experiments. The highlighted region in the figure represents data that was heavily affected by UHSAS saturation, leading to suppressed deposition rates. Data in this region is omitted from the modeled deposition analysis.

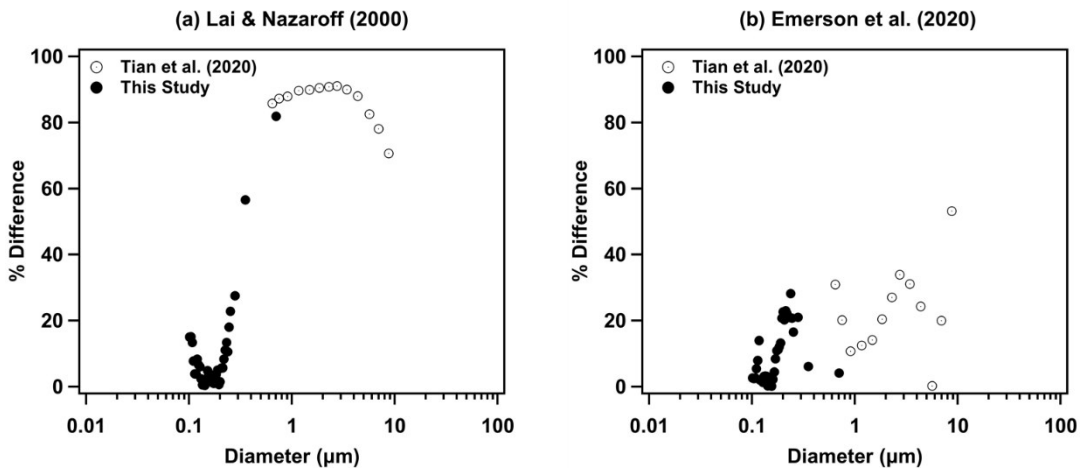

Figure S14: Percent difference between the modeled and measured deposition velocities and rates for the **(a)** Lai and Nazaroff (2000) indoor model and **(b)** Emerson et al. (2020) outdoor model.[3,5] These residuals were calculated for the UHSAS data and the deposition rate values from Tian et al. (2020).[15]

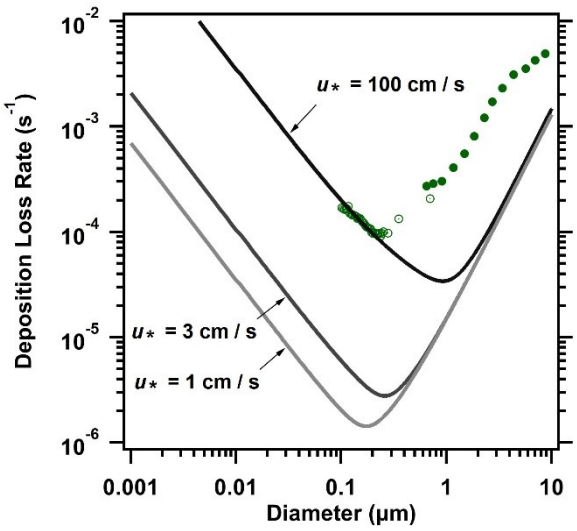

Figure S15: Deposition loss rates produced by different friction velocities in the Lai and Nazaroff (2000) model.[3] Green points represent the UHSAS data (open circles) and the deposition rate data presented in Tian et al. (2020) (closed circles) from the HOMEChem study.[15]

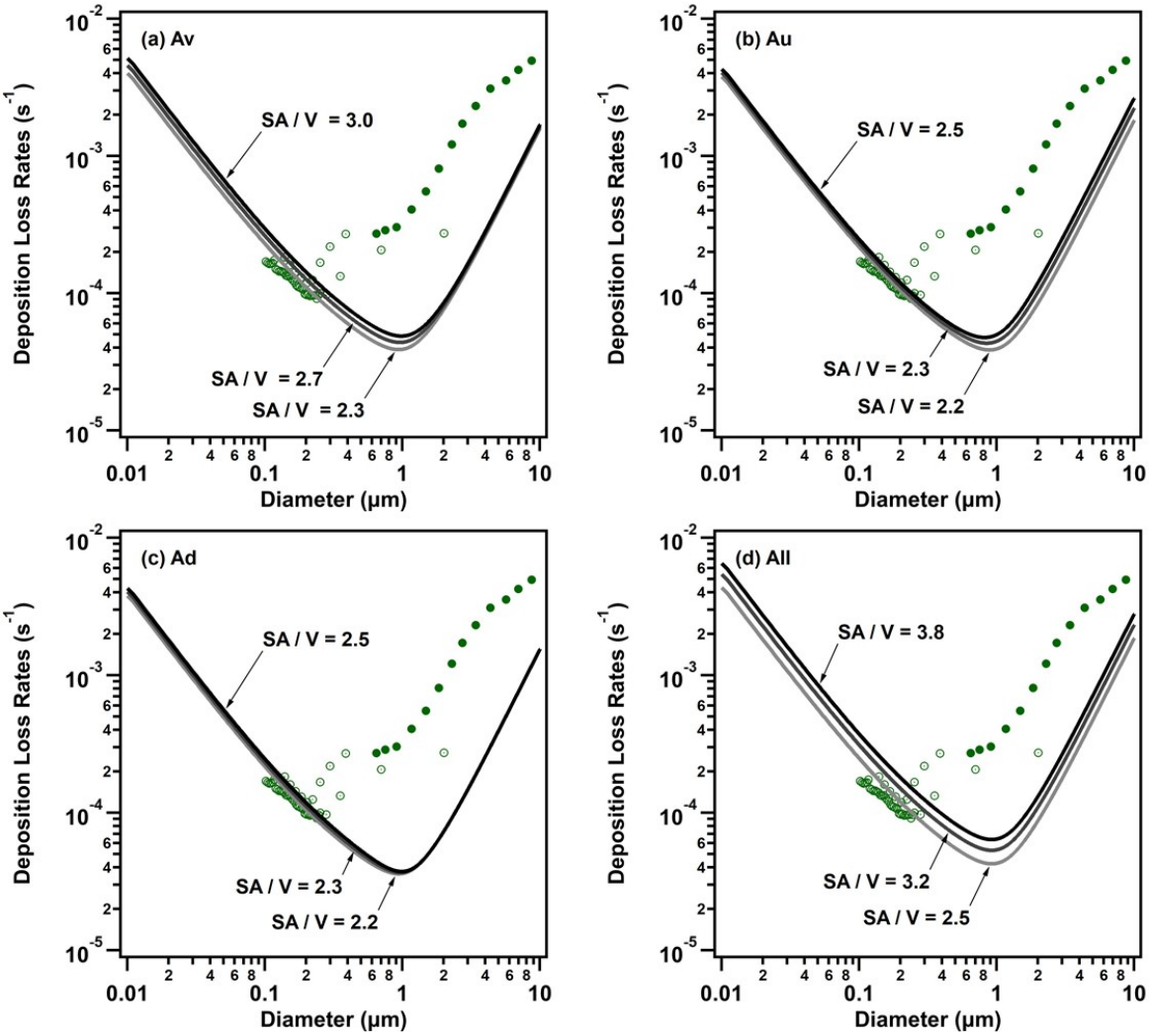

Figure S16: Constraint of the surface-area-to-volume ratio (SA/V) in the Lai and Nazaroff (2000) model.[3] Surface area was increased by 20% (light grey line), 50% (grey line), and 80% (black line) for the **(a)** vertical surfaces, **(b)** upward-facing surfaces, **(c)** downward-facing surfaces, and **(d)** all surfaces. In all cases volume was decreased by 10% from the reported volume for the test house. This manipulation was based on the work of Manuja et al. (2019), where it was reported that on average the contents of a room result in a 50% increase in the total surface area and a 10% decrease in the total volume.[16] None of these variations in the surface-area-to-volume ratio had a significant impact on the agreement between the observed deposition rates and those produced by the model. Green points represent the UHSAS data (open circles) and the deposition rate data presented in Tian et al. (2020) (closed circles) from the HOMEChem study.[15]

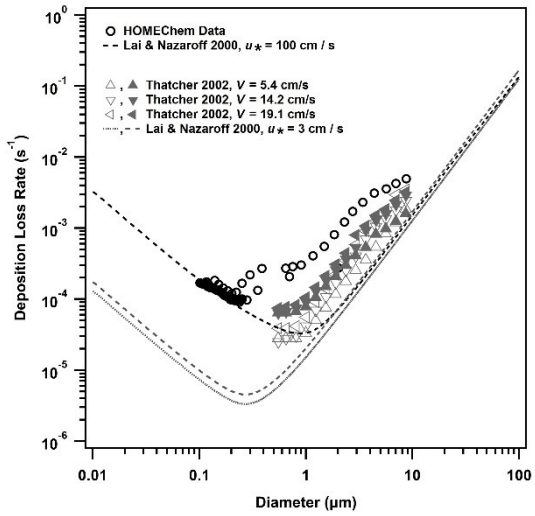

Figure S17: Comparison between the values and model parameters found in Thatcher et al. (2002) (open markers are bare room and closed markers are for a furnished room)and the values obtained during HOEMChem. The HOMEChem deposition measurements lie within the range of variability for indoor measurements that Thatcher et al. (2002) explored and found similar underestimation of deposition from the Lai and Nazaroff (2000) model[3,17]. All model runs assume unit density (1.0 g cm^{-3}) in this figure.

S7.3: Coagulation during cooking

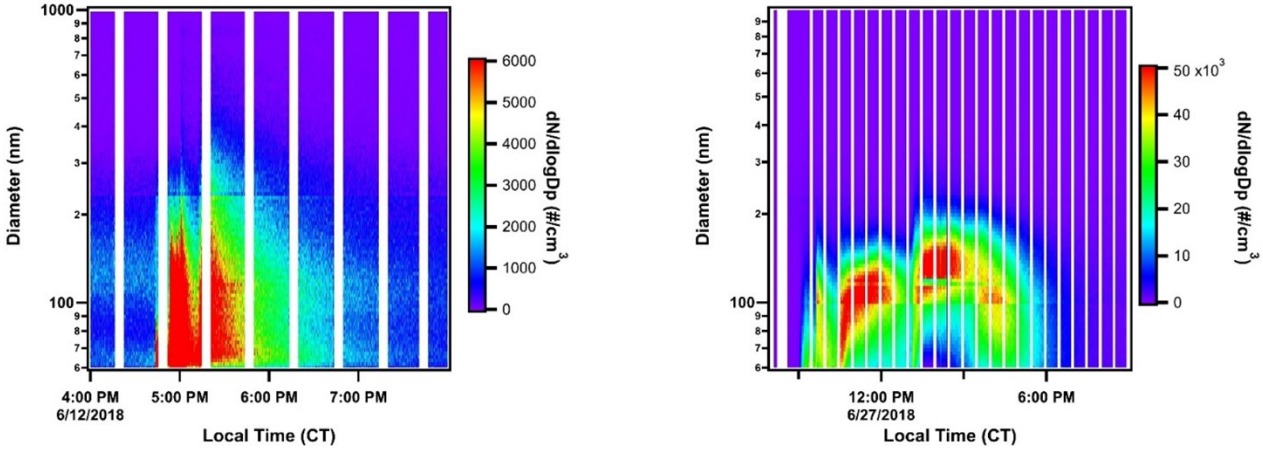

Figure S18: Concentration map for a typical stir-fry event (left) and one of the Thanksgiving Day experiments (right). Coagulation was not a major loss mechanism for particles produced during pulsed events, however, when concentration was high for an extended period, like it was during Thanksgiving, coagulation was observed.

Table S11: Major equations used in coagulation calculations, following Fuchs form of the Brownian coagulation coefficient.[18]

Parameters	Equation

Diffusivity (D_i)*	$D = \dfrac{k_B T\, C_C}{3\,\pi\,\mu\, d_{p,i}}$
Mean thermal speed of the particle ($\bar{c}_i$)**	$\bar{c}_i = \left(\dfrac{8\, k_B\, T}{\pi\, m_i}\right)^{1/2}$
Mean free path (l_i)	$l_i = \dfrac{8\, D_i}{\pi\, \bar{c}_i}$
Gravitational constant (g_i)	$g_i = \dfrac{1}{3\, d_{p,i}\, l_i}\left[\left(d_{p,i} + l_i\right)^3 - \left(d_{p,i}{}^2 + l_i{}^2\right)^{3/2}\right] - d_{p,i}$
Coagulation coefficient ($K_{i,j}$)	$K_{1,2} = 2\pi\left(D_1 + D_2\right)\left(d_{p,1} + d_{p,2}\right)\left(\dfrac{d_{p,1} + d_{p,2}}{d_{p,1} + d_{p,2} + 2\left(g_1^2 + g_2^2\right)^{1/2}} + \dfrac{8\,(D_1 +}{\left(\bar{c}_1^2 + \bar{c}_2^2\right)^{1/2}(}\right.$

* The variable C_c is the Cunningham slip correction factor and μ is the viscosity of air.
** The variable m_i is the mass of particle i.

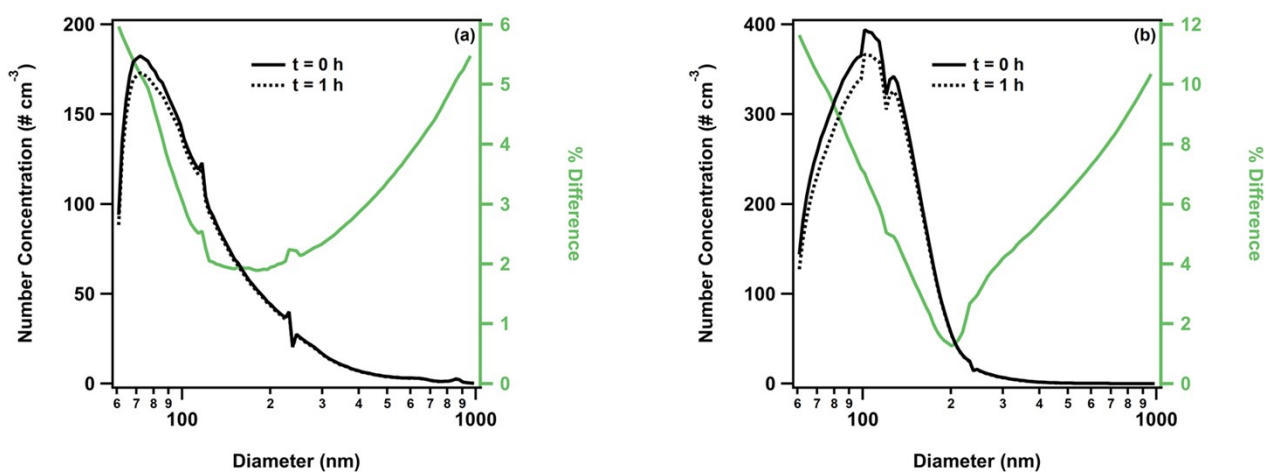

Figure S19: Results of theoretical calculations for the impact of coagulation on **(a)** stir-fry (total starting concentration of 5197 # cm^{-3}) and **(b)** Thanksgiving Day experiments (total starting concentration of 11813 # cm^{-3}). In both panels, the average distribution for the experiments is represented as the solid black line (t = 0), and the predicted distribution after having coagulation as the only loss process for 1 hour is the dashed black line. Percent difference between the two distributions, on the right axis, is displayed in green.

Section S7: Observed gradients in aerosol concentration during cooking

Table S12: Statistical data (maximum, 75th percentile, median, 25th percentile, and minimum) for the percent differences between the kitchen and the living room during cooking. Absent numbers in the larger bins are a result of excluding data where concentration was less than 1 # cm^{-3}.

Mean Diameter (µm)	Maximum	75th	Median	25th	Minimum
139.32	89.25	65.78	44.16	31.16	16.64
152.41	88.29	68.49	54.92	38.98	33.61
167.49	84.87	75.10	52.01	42.40	36.79
184.50	84.29	73.85	46.59	39.65	32.05
202.54	83.38	66.15	48.23	39.21	34.83
222.08	80.54	44.90	37.50	27.54	18.27
251.77	72.47	30.31	18.35	12.43	3.92
298.54	109.89	73.37	59.06	22.75	8.29
387.26	74.71	35.42	27.70	6.32	1.08
522.99	47.29	38.59	26.91	8.45	0.38
764.72	70.03	44.90	24.21	21.05	1.19
1132.40	121.47	75.811	42.03	17.33	5.41
1399.59	77.92	58.14	30.75	20.52	17.91
1627.42	81.90	81.90	43.70	5.50	5.50
2157.74	-	-	-	-	-
3002.62	-	-	-	-	-

Table S13: Statistical data (maximum, 75th percentile, median, 25th percentile, and minimum) for the percent differences between the kitchen and the bedroom during cooking. Absent numbers in the larger bins are a result of excluding data where concentration was less than 1 # cm^{-3}.

Mean Diameter (µm)	Maximum	75th	Median	25th	Minimum
139.32	93.56	82.43	71.16	56.83	39.92
152.41	96.46	86.45	70.95	62.87	43.45
167.49	97.61	82.03	72.49	63.75	42.02
184.50	97.34	74.38	69.03	61.17	34.42
202.54	96.43	72.59	63.72	57.26	31.12
222.08	95.42	72.25	59.95	53.28	32.10
251.77	91.87	60.92	36.41	20.66	4.50
298.54	86.64	54.14	39.32	22.94	1.29
387.26	90.26	66.60	56.00	35.06	7.01
522.99	85.65	67.93	60.28	47.95	1.29
764.72	72.58	60.73	49.74	34.01	10.99
1132.40	76.85	58.64	50.77	34.36	8.66
1399.59	77.19	56.53	29.61	14.55	5.74
1627.42	74.08	74.08	38.84	3.61	3.61
2157.74	-	-	-	-	-
3002.62	-	-	-	-	-

References

1 B. J. Turpin and H.-J. Lim, Species Contributions to PM2.5 Mass Concentrations: Revisiting Common Assumptions for Estimating Organic Mass, *Aerosol Sci. Technol.*, 2001, **35**, 602–610.

2 S. Patel, S. Sankhyan, E. K. Boedicker, P. F. DeCarlo, D. K. Farmer, A. H. Goldstein, E. F. Katz, W. W. Nazaroff, Y. Tian, J. Vanhanen and M. E. Vance, Indoor Particulate Matter during HOMEChem: Concentrations, Size Distributions, and Exposures, *Environ. Sci. Technol.*, 2020, **54**, 7107–7116.

3 A. C. K. Lai and W. W. Nazaroff, Modeling Indoor Particle Deposition from Turbulent Flow onto Smooth Surfaces, *J. Aerosol Sci.*, 2000, **31**, 463–476.

4 D. K. Farmer, M. E. Vance, J. P. D. Abbatt, A. Abeleira, M. R. Alves, C. Arata, E. Boedicker, S. Bourne, F. Cardoso-Saldaña, R. Corsi, P. F. DeCarlo, A. H. Goldstein, V. H. Grassian, L. H. Ruiz, J. L. Jimenez, T. F. Kahan, E. F. Katz, J. M. Mattila, W. W. Nazaroff, A. Novoselac, R. E. O'Brien, V. W. Or, S. Patel, S. Sankhyan, P. S. Stevens, Y. Tian, M. Wade, C. Wang, S. Zhou and Y. Zhou, Overview of HOMEChem: House Observations of Microbial and Environmental Chemistry, *Environ. Sci. Process. Impacts*, 2019, **21**, 1280–1300.

5 E. W. Emerson, A. L. Hodshire, H. M. DeBolt, K. R. Bilsback, J. R. Pierce, G. R. McMeeking and D. K. Farmer, Revisiting particle dry deposition and its role in radiative effect estimates, *Proc. Natl. Acad. Sci.*, , DOI:10.1073/pnas.2014761117.

6 L. Zhang, S. Gong, J. Padro and L. Barrie, A size-segregated particle dry deposition scheme for an atmospheric aerosol module, *Atmos. Environ.*, 2001, **35**, 549–560.

7 Q. Y. Meng, D. Spector, S. Colome and B. Turpin, Determinants of indoor and personal exposure to PM2.5 of indoor and outdoor origin during the RIOPA study, *Atmos. Environ.*, 2009, **43**, 5750–5758.

8 E. Abt, H. H. Suh, G. Allen and P. Koutrakis, Characterization of Indoor Particle Sources: A Study Conducted in the Metropolitan Boston Area, *Environ. Health Perspect.*, 2000, **108**, 35–44.

9 J. Kearney, L. Wallace, M. MacNeill, X. Xu, K. VanRyswyk, H. You, R. Kulka and A. J. Wheeler, Residential indoor and outdoor ultrafine particles in Windsor, Ontario, *Atmos. Environ.*, 2011, **45**, 7583–7593.

10 J. Kearney, L. Wallace, M. MacNeill, M.-E. Héroux, W. Kindzierski and A. Wheeler, Residential infiltration of fine and ultrafine particles in Edmonton, *Atmos. Environ.*, 2014, **94**, 793–805.

11 C. M. Long, H. H. Suh, P. J. Catalano and P. Koutrakis, Using Time- and Size-Resolved Particulate Data To Quantify Indoor Penetration and Deposition Behavior, *Environ. Sci. Technol.*, 2001, **35**, 2089–2099.

12 R. Allen, T. Larson, L. Sheppard, L. Wallace and L.-J. S. Liu, Use of Real-Time Light Scattering Data To Estimate the Contribution of Infiltrated and Indoor-Generated Particles to Indoor Air, *Environ. Sci. Technol.*, 2003, **37**, 3484–3492.

13 J. Zhao, W. Birmili, B. Wehner, A. Daniels, K. Weinhold, L. Wang, M. Merkel, S. Kecorius, T. Tuch, U. Franck, T. Hussein and A. Wiedensohler, Particle Mass Concentrations and Number Size Distributions in 40 Homes in Germany: Indoor-to-outdoor Relationships, Diurnal and Seasonal Variation, *Aerosol Air Qual. Res.*, 2019, **20**, 576–589.

14 T. Hussein, K. Hämeri, M. S. A. Heikkinen and M. Kulmala, Indoor and outdoor particle size characterization at a family house in Espoo–Finland, *Atmos. Environ.*, 2005, **39**, 3697–3709.

15 Y. Tian, C. Arata, E. Boedicker, D. M. Lunderberg, S. Patel, S. Sankhyan, K. Kristensen, P. K. Misztal, D. K. Farmer, M. Vance, A. Novoselac, W. W. Nazaroff and A. H. Goldstein, Indoor Emissions of Total and Fluorescent Supermicron Particles during HOMEChem, *Indoor Air*, , DOI:https://doi-org.ezproxy2.library.colostate.edu/10.1111/ina.12731.
16 A. Manuja, J. Ritchie, K. Buch, Y. Wu, C. M. A. Eichler, J. C. Little and L. C. Marr, Total surface area in indoor environments, *Environ. Sci. Process. Impacts*, 2019, **21**, 1384–1392.
17 T. L. Thatcher, A. C. K. Lai, R. Moreno-Jackson, R. G. Sextro and W. W. Nazaroff, Effects of room furnishings and air speed on particle deposition rates indoors, *Atmos. Environ.*, 2002, **36**, 1811–1819.
18 J. H. Seinfeld and S. N. Pandis, *Atmospheric Chemistry and Physics: From Air Pollution to Climate Change*, John Wiley & Sons, Inc., New York, NY, 3rd edn., 1998.